Chinese Society of Aeronautics and Astronautics
& Beihang University

Chinese Journal of Aeronautics

Image motion and experimental study of a 0.1″ space pointing measuring instrument for micro-vibration conditions

Lin LI [a,b,*], **Li YUAN** [a,b,c], **Li WANG** [a,b], **Miaomiao WANG** [a,b], **Xiaoxue GONG** [d,e,f], **Jie SUI** [a,b], **Yanpeng WU** [a,b], **Ran ZHENG** [a,b]

[a] *Space Optoelectronic Measurement and Perception Lab., Beijing Institute of Control Engineering, Beijing 100190, China*
[b] *China Academy of Space Technology, Beijing 100094, China*
[c] *Science and Technology on Space Intelligent Control Laboratory, Beijing 100094, China*
[d] *University of Chinese Academy of Sciences, Beijing 100049, China*
[e] *Changchun Institute of Optics, Fine Mechanics and Physics, Chinese Academy of Sciences, Changchun 130033, China*
[f] *Chang Guang Satellite Technology Co., Ltd., Changchun 130102, China*

Abstract There exists an increasing need for Milli-Arc-Seconds (MAS) accuracy pointing measurement for current and future space systems. To meet the 0.1″ space pointing measurement accuracy requirements of spacecraft in future, the influence of spacecraft micro-vibration on a 0.1″ Space Pointing Measuring Instrument (SPMI) is studied. A Quasi-Zero Stiffness Device (QZSD) with adaptive adjustment and variable stroke was proposed. Then, a series of micro-vibration experiments of the SPMI were carried out. The influence of the micro-vibration generated by Guidance Navigation Control (GNC) attitude control components under different attitudes on the SPMI was analyzed. Point spread function of image motion in micro-vibration was also derived. Further, the changes of image motion under the micro-vibration environment were evaluated by extracting the gray centroid of the images, and the experiment processes and results are deeply discussed. The results show that the first-order frequency of the QZSD system is 0.114 Hz, and it is induced by a double pendulum system; the image motion of single flywheel spinning reached 0.015 pixels; whilst the image motion reached 0.03

---

* Corresponding author at: Space Optoelectronic Measurement and Perception Lab., Beijing Institute of Control Engineering, Beijing 100190, China.
E-mail address: cast_lilin@163.com (L. LI).

Production and hosting by Elsevier

1. Introduction

Space pointing measurement is a technology to measure the attitude or Line of Sight (LOS) of spacecraft or pay-load in reference coordinate system.[1,2] The measurement instruments include star sensor, star camera and target tracking camera, which generally referenced by celestial body.[1] With their help, the pointing parameters can be calculated by image processing of the image of the obtained space target images.

It will be a big benefit[3] to space optical communication, gravitational wave detection, inter-satellites measurement, accurately landing for celestial bodies if spacecraft pointing accuracy reached 0.1″ or higher. However, this is a challenge because MAS-SPMI systems are very sensitive to disturbances, such as micro-vibrations that generated by the components of spacecraft GNC system.[4–7] Most spacecraft will be affected by micro-vibration, low-level mechanical vibration or disturbance in the microgravity environment, typically occurring at frequencies of less than 1 Hz up to a few kHz.[7] For the low amplitude of the micro-vibration dynamic environment, it has no obvious impact on most components of the spacecraft, so it is usually negligible.[2] However, for MAS-SPMI, the micro-vibration environment seriously affects the pointing accuracy, and sharply produces unwanted image motion,[8] thus affecting pointing measurement accuracy. Therefore, the impact of micro-vibration must be considered in the development of 0.1″ spacecraft. Modeling analysis and experimental studies are effective methods for micro-vibration research.[2] Due to the complexity of multi excitation coupling and structural resonance in the process of micro-vibration transmission in spacecraft structure, modeling analysis method produce significant error, which may reach about 50%.[9–13] The experimental study method is much more accurate, and the error is usually less than 10%.[4,5,9,13] Yet, the low stiffness for micro-vibration experiment in laboratory has provided this much needed foundation, especially how to ensure quasi-zero stiffness environment is seriously important, which will be one of the key factors to determine the reliability of the experiment.[14–16]

Pasting acceleration sensor at the sensitive position of spacecraft structure to measure the magnitude of disturbance is suitable for micro-vibration test, and multiple sensors could be pasted to collect disturbance data from differential locations.[17–18] However, this method has a high location accuracy requirement for the acceleration sensors, and the mass of sensors will have a certain impact on the optical structure, in addition, the micro-vibration response measured by the sensor cannot directly establish the decrement of the image. Using laser to measure micro-vibration is a relatively mature non-contact testing method, which is usually tested by using Doppler frequency shift or laser interference technology.[17–19] This method may not have an adverse impact on the tested system in the measurement process. Nevertheless, for well-equipped instruments, it is not possible to measure the disturbance of its internal structure and image motion. Direct imaging method evaluates the influence of micro-vibration by analyzing image parameters, such as image motion, through imaging experiments. This method requires the test system to have quasi-zero stiffness condition. Flexible rope was mostly used to realize the low stiffness in the process of micro-vibration test.[20–23] Even so, the stiffness of flexible-rope methods is still larger and do not have the ability of displacement adjustment and direction adjustment.

Based on the suspension method, a Quasi-Zero Stiffness Device (QZSD), with adaptive adjustment and variable stroke is proposed, it can be simplified as a double pendulum system, and effectively realize the low stiffness environment required for the micro-vibration test of MAS-SPMI systems. Furthermore, the changes of image motion under the micro-vibration environment of different spacecraft attitudes were evaluated by extracting the gray centroid of the images, and the experiment process and results are discussed in-depth. Contents of this paper are divided in to five parts. Section 1 is the introduction. Section 2 introduces the compositions of the experiment systems in-detail. Section 3 mainly focuses on the principles. Section 4 studies experimental process and discuss the results. The last section concludes the research work of this paper. This work provides an effective technical support for the development of spacecraft with milli-arc-seconds pointing requirements.

2. Experiment systems

2.1. System components

The micro-vibration experiment system mainly includes integrating sphere, aperture target, collimator, pointing measuring instrument of 0.1″, quasi-zero stiffness device, flywheels, equivalent platform about inertia moment, optical vibration isolation platform and controllers. The micro-vibration imaging experiment system is shown schematically in Fig. 1. The integrating sphere, aperture target and collimator are installed on the optical vibration isolation platform. The pointing measuring instrument is the measured object, and MAS-SPMI is fixedly connected with the equivalent platform; three flywheels are orthogonally installed on the equivalent platform to provide low mechanical disturbance for the pointing measuring instrument; the QZSD is providing low stiffness, which is one of the core condition; and the quasi-zero stiffness suspension adjusting device, pointing measuring instrument, disturbance source and inertia equivalent platform form a set of two pendulum system. Note that, D is the diameter of the collimator, and f is the focal length of collimator.

2.2. Quasi-zero stiffness device components

The QZSD consists of suspension crown block, high stiffness sling, slings for lifting loads, spring with high strength and high
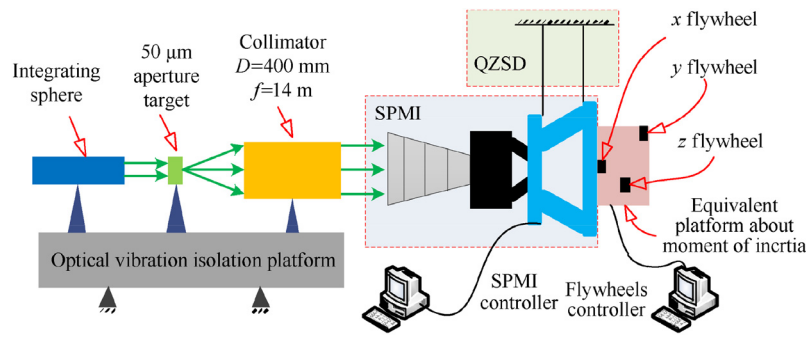
Fig. 1 Schematic diagram of experiment system.

strength, bidirectional bolts, as shown in Fig. 2. The slings for lifting loads are placed horizontally, four second lifting points are set at the four corners of the upper end face, and four third lifting points are set at the four corners of the lower end face. Four second lifting points are respectively connected to the suspension crown block through the high stiffness sling, and the four third lifting points are respectively connected to the upper end of the corresponding spring under the slings for lifting loads through the high stiffness slings; The lower ends of the four springs are respectively connected to the first lifting point through a bidirectional bolt. The top of the equivalent platform about inertia moment is provided with four hooks, which are respectively connected with the four first lifting points at the lower end of QZSD; The bidirectional bolts consist of a two-sided nut frame and two M16 high-strength bolts. After the equivalent platform suspended, adjust the direction of six degrees of freedom (x, y, z, u, v, w) through QZSD, so that the pointing measuring instrument is facing the collimator, where the coordinate system is defined in Fig. 3.

2.3. Coordinates

The coordinate system of experiment system is defined, as shown in Fig. 3. The coordinate origin point of the experiment coordinate system is located at the center of mass pointed to the SPMI, the moment of inertia equivalent platform and

the flywheel assembly. It is defined that the optical axis direction is the positive axis in z axis, x axis and y axis are parallel to the image plane; the pitch direction of the test system is around the x axis, the yaw direction is around the y axis, and the roll direction is around the z axis.

The origin coordinate O_f is located at the center of the focal plane pointed to SPMI. The normal direction of the focal plane is defined as the positive axis of z_f, which coincides with the optical axis z. The x_f axis and y_f axis are parallel to the x axis and y axis of the experiment system coordinate system respectively. The distance between the origin point O of the experiment system coordinate system and the origin point O_f of the focal plane coordinate system is 208.3 mm. Point $p(\theta, L)$ represents the real position of the aperture target on the focal plane under the micro-vibration environment, θ represents the image motion direction, and L represents the image motion value.

3. Principles

3.1. Quasi-zero stiffness

In this paper, the quasi-zero stiffness design of the test device is completed by the four groups of springs and high stiffness slings. It is assumed that each group of spring ropes contains
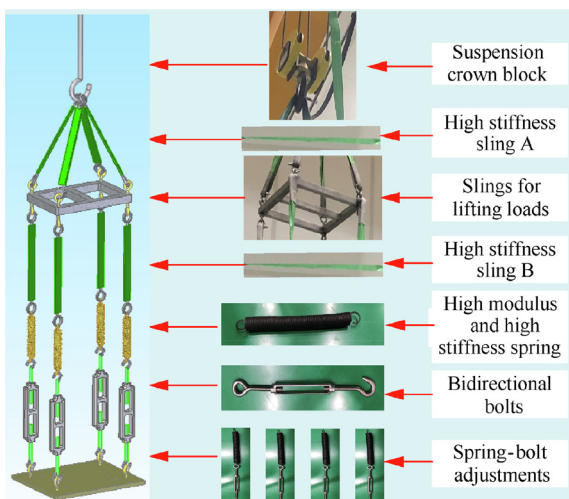

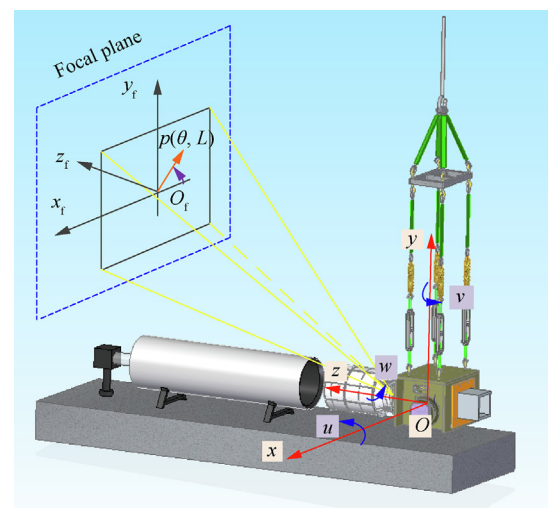**Fig. 2** Schematic diagram of quasi zero stiffness devices.

Fig. 3 Schematic diagram of experiment system coordinate.

the same number of linear springs and share the total mass m_s (about 110 kg), including SPMI, test tooling, disturbance sources, quasi-zero stiffness device and other connecting fasteners. A previous work[15] and Refs. 20–23 have shown that experiment system stiffness can be calculated by approximately regarding the suspension system as a single pendulum system to calculate the system stiffness. However, in this work, we found that the quasi-zero stiffness device, SPMI, disturbance source and inertia equivalent platform form a set of double pendulum system. There exists a great impact on the stiffness calculation of the test system.

The dynamic equation of the double pendulum system is established by LaGrange equation.[24] The equation is a system of binary second-order implicit differential equations, which is solved by Runge-Kutta method[25] to obtain the characteristic frequency of the device, that is, the stiffness value of the experiment system.

The dynamic equation of the double pendulum system is expressed by

$$\begin{cases} L_1\ddot{\theta}_1 + \frac{m_2}{(m_1+m_2)}L_2\ddot{\theta}_2\cos(\theta_2-\theta_1) - \frac{m_2}{(m_1+m_2)}L_2\ddot{\theta}_2\sin(\theta_2-\theta_1) \\ +g\sin\theta_1 = 0 L_2\ddot{\theta}_2 + L_1\ddot{\theta}_1\cos(\theta_2-\theta_1) - L_1\ddot{\theta}_1\sin(\theta_2-\theta_1) \\ +g\sin\theta_2 = 0 \end{cases}$$
(1)

where L_1 is the length of the first swing arm, L_2 is the length of the second swing arm, m_1 is the equivalent mass of the first swing arm, m_2 is the equivalent mass of the second swing arm, and g is the gravitational acceleration in direction, θ_1 is the included angle between the first swing arm and the gravitational acceleration in direction, θ_2 is the included angle between the second swing arm and the gravitational acceleration in direction; $\ddot{\theta}_1$ represent the second derivative of θ_1, and $\ddot{\theta}_2$ represent the second derivative of θ_2.

Runge-Kutta method is used for solving Eq. (1). The first two-order frequencies caused by the double pendulum system are 0.1137 Hz and 0.2953 Hz, respectively, as shown in Fig. 4.

3.2. Variable stroke and double stroke adjustment principle

To ensure the image of the aperture target is limited in image focal plane of SPMI during the installation and adjustment of the experiment system, the pitch and yaw attitude would be
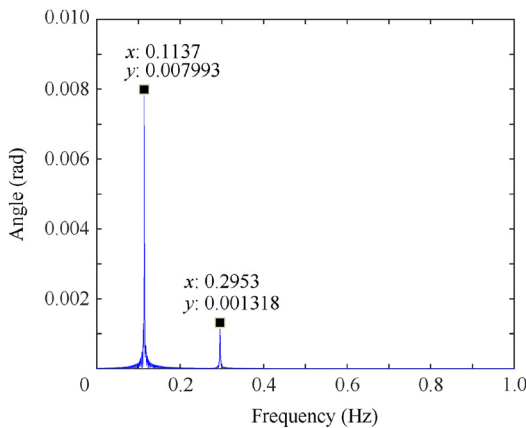

Fig. 4 Results of θ_1 and θ_2.

adjusted through the double range bolts component to make the target image in the field of view of SPMI. The pitch of M16 bolt is one millimeter, which means that the double pass bolt rotates for one turn, and the change value Z_u at both ends of the bolt is two millimeters. Based on this principle, the adjustment resolution of single turn θ_u is calculated as follows:

$$\theta_u = \frac{Z_u}{A} \cdot \frac{180}{\pi}$$
(2)

If the single circle scale is divided into sixty parts, then

$$Z'_u = Z_u/60$$
$$\theta'_u = \frac{\theta_u}{60}$$
(3)

During the experiment progress, the aperture target can be adjusted within the field of view of SPMI easily in a short time through the double range bolt.

3.3. Image motion mechanism caused by micro-vibration

The micro-vibration of spacecraft includes six degrees of freedom, which are embodied in three degrees of freedom linear micro-vibration and three degrees of freedom angular micro-vibration. The dynamic imaging process of space point target is usually described by Point Spread Function (PSF),[26] which is expressed by

$$\delta(x,y) = s(x,y)\prod_{i=1}^{6} d_i(x,y) + g(x,y)$$
(4)

where $\delta(x,y)$ represents the target imaging in the micro-vibration environment, $s(x,y)$ represents the image in the undisturbed environment, $\prod_{i=1}^{6} d_i(x,y)$ represents the point spread function PSF in the micro-vibration environment in the six degrees of freedom direction, and $g(x,y)$ is Gaussian white noise.

In the micro-vibration environment, the point spread function and its Fourier Transformation $D(u,v)$ is respectively expressed as follows:

$$d(x,y) = \begin{cases} 1/L, & x \in [0,L\cos\theta], y \in [0,L\sin\theta] \\ 0, & \text{otherwise} \end{cases}$$
(5a)

$$D(u,v) = \frac{\sin(\Pi(u\cos\theta + v\sin\theta)L)}{\Pi(u\cos\theta + v\sin\theta)L}e^{-j\Pi(u\cos\theta+v\sin\theta)L}$$
(5b)

Therefore, the PSF could be further described in micro-vibration environment.

3.3.1. PSF of linear micro-vibration
The linear micro-vibration is decomposed into three axes, x axis, y axis and z axis. The linear micro-vibration on the optical axis z axis will not cause the position change of the point target on the image plane, and its value is zero, i.e.:

$$L_z = 0$$
(6)

In the image plane, the x axis and y axis are orthogonal and symmetrical, and their influence mechanism is the same, as shown in Fig. 5.

From the Triangular geometric relationship:
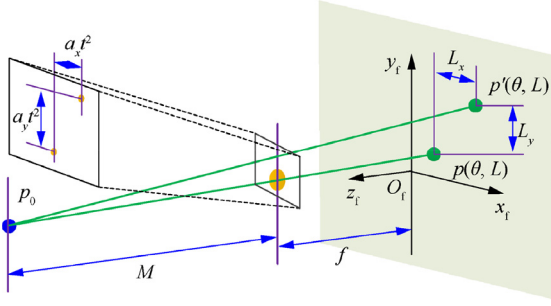
$$\frac{M}{M+f} = \frac{at^2}{L}$$
(7)

Fig. 5   Schematic diagram of line micro-vibration.

where, M represents the object distance, f represents the focal length of SPMI, a represents the acceleration caused by micro-vibration, and t represents the acceleration duration time.

Then, the point spread function of linear micro-vibration can be expressed as

$$\begin{cases} L_x = (1 + f/M)a_x t^2, \ \theta = 0° \\ L_y = (1 + f/M)a_y t^2, \ \theta = 90° \\ L_z = 0 \end{cases} \tag{8}$$

3.3.2. PSF of angular micro-vibration around LOS

The influence of angular micro-vibration around the optical axis z axis on imaging is different from that of non-optical axis. Due to the relativity of motion, when the incident light remains unchanged, the angular micro-vibration $\Delta\gamma$ of the pointing measuring instrument around z axis can be equivalent to the angular micro-vibration $\Delta\gamma$ of the incident light around z axis when the absolute position of SPMI remains unchanged, as shown in Fig. 6.

As shown in Fig. 5, the image point $p(\theta, L)$ moves to point $p'(\theta, L)$ after angular vibration. According to the linear micro-vibration derivation method, the PSF of angular micro-vibration around the optical axis in a short exposure time is expressed as formula (9), α_w is the angular acceleration around the z_f.

$$L_w = \sqrt{x^2 + y^2}\,\alpha_w t^2, \theta = \pi/2 + \arctan(y/x) \tag{9}$$

3.3.3. PSF of angular micro-vibration vertical LOS

The x axis and y axis are in the direction of non-optical axis. The angular micro-vibration along the non-optical axis will cause the image plane, incident light and optical axis to rotate around the non-optical axis, and make the imaging image
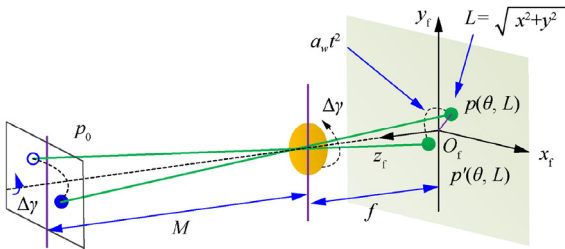
points offset. This relative motion is equivalent to the immobility of the optical center. The angular micro-vibration generated by the image plane, incident light and the optical axis around the image plane x axis is of $\Delta\phi$ and $\Delta\varphi$ of y axis, as shown in Fig. 7.

The PSF of angular micro-vibration around x axis and y axis can be obtained as follows:

$$\begin{cases} L_u = \frac{f^2 + x^2}{f}\alpha_u \cdot t^2, \ \theta = 0° \\ L_v = \frac{f^2 + y^2}{f}\alpha_v \cdot t^2, \ \theta = 90° \end{cases} \tag{10}$$

3.4. Extraction method of image motion caused by micro-vibration

Under the influence of flywheel disturbance, the image motion is the main factor that makes the accuracy worse. In this paper, the image gray value centroid is used as the evaluation reference of image motion. The calculation formula of centroid algorithm is shown as follows:

$$x_k = \frac{\sum_{j=1}^{m}\sum_{i=1}^{n}I_{ij}i}{\sum_{j=1}^{m}\sum_{i=1}^{n}I_{ij}} \tag{11a}$$

$$y_k = \frac{\sum_{j=1}^{m}\sum_{i=1}^{n}I_{ij}j}{\sum_{j=1}^{m}\sum_{i=1}^{n}I_{ij}} \tag{11b}$$

where I_{ij} represents the gray value of pixel points in i row and j column, x_k is the coordinate of the gray value centroid of the k-th frame image in x direction of the image plane, is the coordinate of the gray value centroid of the k-th frame image in the y direction of the image plane.

Before extract the energy center of the light spot by Eqs. (11a) and (11b), there is a very important progress to improve the calculation accuracy, that is, system noise calibration. The gray value error of each CCD pixel is calibrated from serial image data obtained in dark test field.

The gray value of the tested imaging picture is subtracted from the gray value of the static dark field picture before test to eliminate the static dark field noise error of the system. In addition, to reduce the error caused by the pixel gray value error on the solution of the energy center, this paper sets the gray values of all pixels outside the bright spot area with a size of no more than 10×10 pixels to zero before calculating the image energy center. Then, Eq. (11) can be rewritten as

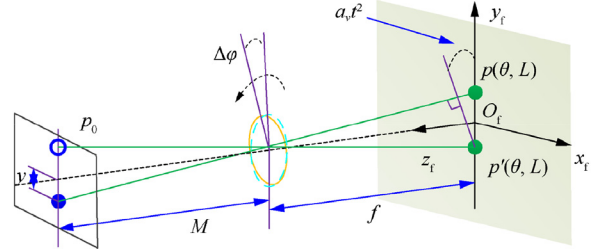**Fig. 6**   Schematic diagram of angular micro-vibration around z axis.

Fig. 7   Schematic diagram of angular micro-vibration around x axis or y axis.

$$x_k = \frac{\sum_{j=j_0}^{j_0+10}\sum_{i=i_0}^{i_0+10} I_{ij}^k i}{\sum_{j=j_0}^{j_0+10}\sum_{i=i_0}^{i_0+10} I_{ij}^k}$$

$$= i_0 + \frac{\sum_{j=j_0}^{j_0+10}\sum_{i=i_0+1}^{i_0+10} I_{ij}^k + \cdots + \sum_{j=j_0}^{j_0+10}\sum_{i=i_0+10}^{i_0+10} I_{ij}^k}{\sum_{j=j_0}^{j_0+10}\sum_{i=i_0}^{i_0+10} I_{ij}^k} \tag{12a}$$

$$y_k = \frac{\sum_{i=i_0}^{i_0+10}\sum_{j=j_0}^{j_0+10} I_{ij}^k j}{\sum_{j=j_0}^{j_0+10}\sum_{i=i_0}^{i_0+10} I_{ij}^k}$$

$$= j_0 + \frac{\sum_{i=i_0}^{i_0+10}\sum_{j=j_0+1}^{j_0+10} I_{ij}^k + \cdots + \sum_{i=i_0}^{i_0+10}\sum_{j=j_0+10}^{j_0+10} I_{ij}^k}{\sum_{j=j_0}^{j_0+10}\sum_{i=i_0}^{i_0+10} I_{ij}^k} \tag{12b}$$

4. Experiments and discussion

4.1. Experiments and results

According to Fig. 1, the micro-vibration test site environment of SPMI was built, and the test process was carried out in a million-level clean laboratory, as shown in Fig. 8(a). The typical image motion diagram under the influence of micro-vibration is shown in Fig. 8(b).

During the experiment progress, the aperture target was adjusted within the field of view of SPMI through the double range bolt. The parameters of quasi-zero stiffness device with adaptive adjustment and variable stroke are calculated as follows according to the Eqs. (2) and (3).

$$\begin{cases} Z_u = 2 \quad \text{mm} \\ \theta_u = \frac{Z_u}{A} \cdot \frac{180}{\pi} = 0.23° \end{cases} \tag{13}$$

The single circle scale was divided into sixty parts, then:

$$\begin{cases} Z'_u = Z_u/60 = 0.03 \quad \text{mm} \\ \theta'_u = \frac{\theta_u}{60} = 0.23' \end{cases} \tag{14}$$

4.1.1. Image motion caused by single-flywheel

By statistical analysis of 3000 near-dark images over the sampling time, gray value skewing caused by system error and random error can be obtained according to the mean and standard deviation of gray value of each pixel. All the values are recorded as an array and applied for gray value offset to eliminate systematic gray value error. Mean value of the stan-

dard deviations is 1.72; it is regarded as standard deviation of the normal distribution obeyed by random gray value error of each pixel.

Firstly, each flywheel was controlled spinning independently to obtain the imaging picture, and the image motion information caused by micro-vibration can be obtained from the picture. Seventeen groups of tests were carried out in increments of 300 r/min from 0 r/min to 4800 r/min. The image processing algorithm in Section 3 is used to solve the centroid position, and the Fourier Transformation is performed to obtain the image shift waterfall plots in frequency domain. The image shift waterfall diagram in frequency domain is shown in Fig. 9.

The calculation results of image motion show that the typical image shift caused by x flywheel and y flywheel are concentrated among the range of 300–400 Hz, among which the image shift caused by y flywheel is the most significant, the image shift peak is 0.01491 pixels in frequency domain, the image shift caused by z flywheel is mainly reflected in the first harmonic of flywheel as shown in Fig. 9(c), and the amplitudes among other frequency bands are smaller.

In Fig. 9(a), the magnitude of image motion caused by x flywheel in both x axis and y axis of the focal plane is at the level of 0.004 pixels. Note that the magnitude of image motion caused by y flywheel in y axis of the focal plane is three times that in x axis, which is at the level of 0.0034 pixels shown in Fig. 9(b). This may indicate that the opti-mechanical system is more sensitive to the micro-vibration produced by y flywheel than in x axis. The image shift caused by z flywheel in Fig. 9(c) further proves this phenomenon.

Typical image motion peaks and frequency in Fig. 9 were extracted shown in Table 1.

4.1.2. Image motion caused by three flywheels coupled

When a spacecraft working in-orbit, it is usually a combination of multiple flywheels spinning to adjust attitude, and micro-vibration may be coupled and nonlinear amplified. To explore whether the mechanical characteristics of micro-vibration can destabilize SPMI when the flywheel rotates at the same time, based on the rotation condition of single flywheel, the characteristic speed with significant influence of each flywheel is selected for combined test. If the influence of each flywheel on imaging meets the linear independent

(a) Micro-vibration experiment site   (b) Typical image motion diagrams under micro-vibration

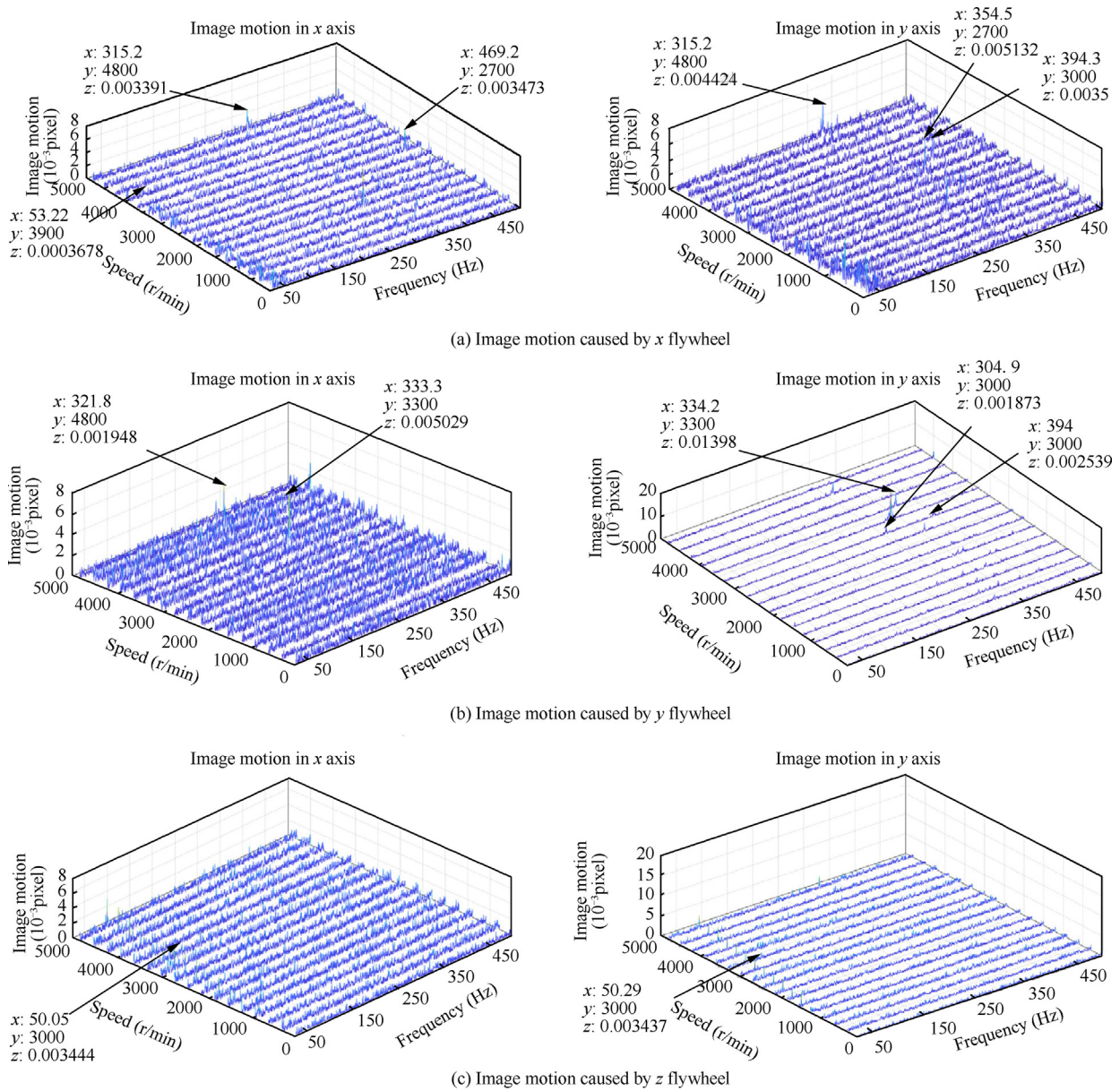**Fig. 8**   Experiment site and typical image motion diagrams.

Image motion in x axis

x: 315.2
y: 4800
z: 0.003391

x: 469.2
y: 2700
z: 0.003473

x: 53.22
y: 3900
z: 0.0003678

Image motion in y axis

x: 354.5
y: 2700
z: 0.005132

x: 315.2
y: 4800
z: 0.004424

x: 394.3
y: 3000
z: 0.0035

(a) Image motion caused by x flywheel

Image motion in x axis

x: 321.8
y: 4800
z: 0.001948

x: 333.3
y: 3300
z: 0.005029

Image motion in y axis

x: 334.2
y: 3300
z: 0.01398

x: 304.9
y: 3000
z: 0.001873

x: 394
y: 3000
z: 0.002539

(b) Image motion caused by y flywheel

Image motion in x axis

x: 50.05
y: 3000
z: 0.003444

Image motion in y axis

x: 50.29
y: 3000
z: 0.003437

(c) Image motion caused by z flywheel

Fig. 9   Waterfall plots of image shift caused by single-flywheel.

Table 1   Typical response information of each flywheel.

Flywheel position	Typical speed (r/min)	Image motion peaks in x axis (pixel@Hz)	Image motion peaks in y axis (pixel@Hz)
x flywheel	2700	0.00347@469.2	0.0051@354.5
	3000		0.0035@394.3
	4800	0.0034@315.2	0.0044@315.2
y flywheel	3000		0.0028@304,0.0025@394
	3300	0.0051@333.3	0.015@334.2
	3600		0.006@364.5
z flywheel	3000	0.0034@50	0.0042@50

Table 2   Nine groups of speed combination conditions.

Number	Flywheel position		
	x flywheel (r/min)	y flywheel (r/min)	z flywheel (r/min)
#1	2700	3000	3000
#2	3000	3000	3000
#3	4800	3000	3000
#4	2700	3300	3000
#5	3000	3300	3000
#6	4800	3300	3000
#7	2700	3600	3000
#8	3000	3600	3000
#9	4800	3600	3000

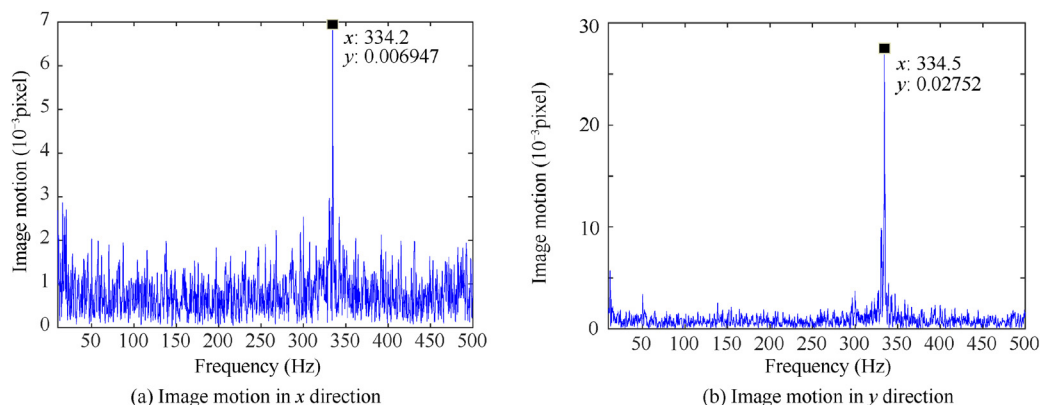(a) Image motion in *x* direction   (b) Image motion in *y* direction

Fig. 10   Image motions in frequency domain @3000 r/min for *x* flywheel, 3300 r/min for *y* flywheel and 3000 r/min for *z* flywheel.

assumption, the image shift under combined working conditions can be obtained by linear superposition of image shifts under single flywheel working conditions.

According to the typical speeds, there are nine groups of speed combination conditions as shown in Table 2 are tested,

and image shift in frequency domain is obtained. The image shift value is the maximum under working conditions of 3000 r/min for *x* flywheel, 3300 r/min for *y* flywheel and 3000 r/min for *z* flywheel. The test results under this worse working condition are shown in Fig. 10. The typical image

Table 3   Typical image motion of linear superposition and combined condition for the nine working conditions.

Number	Image motion peaks in *x* axis (pixel@Hz)		Image motion peaks in *y* axis (pixel@Hz)	
	Linear superposition condition	Combined condition	Linear superposition condition	Combined condition
#1	0.0034@50	0.003@50	0.0038@50	0.0045@50
	0@0	0.0049@324.5	0.0031@303.7	0.0036@303.7
	0@0	0.00395@453.6		0.0052@324.5
			0.0041@354.7	0.00527@354.5
				0.00295@453.6
#2	0.0034@50	0.0029@50	0.0038@50	0.0039@50
			0.0033@304.9	0.005@304
			0.0035@394.3	0.0024@394
#3	0.0034@50	0.0025@50	0.0038@50	0.003@50
	0.0034@315.2	0.0037@314.9	0.003 @303.7	0.0032@304
			0.0039@315.4	0.0052@315.2
#4	0.0034@50	0.0033@50	0.0038@50	0.0023@50
	0.005@333.3	0.0047@333.5	0.014@334	0.014@333.5
			0.004@354.7	0.0028@355
#5	0.0034@50	0.0020@50	0.0038@50	0.0034@50
	0.005@333.3	0.0069@334.2	0.014@334	0.0275@334.5
			0.0035@394.3	0.0023@394
#6	0.0034@50	0.0028@50	0.0038@50	0.003@50
	0.0034@315.2	0.0026@315.4	0.0039@315.4	0.0017@315.2
	0.005@333.3	0.0071@334.5	0.014@334	0.0242@334.5
#7			0.0038@50	0.0036@50
	0.0034@50	0.0032@50		0.0044@308.8
			0.0041@354.7	0.00493@354.5
			0.0063@364.5	0.0065@364.5
#8			0.0038@50	0.0038@50
	0.0034@50	0.004@50		0.0041@309.1
			0.0063@364.5	0.0062@364.7
			0.0035394.5	0.0027@393.3
#9			0.0038@50	0.0029@50
	0.0034@50	0.0048@50		0.004@308.8
			0.0039@315.4	0.0047@314.2
			0.0063@364.5	0.0068@364.2

motion of linear superposition and combined condition for the nine working conditions is shown in Table 3.

The results in Table 3 show that the peak value of image shift response under the combined condition is basically between 300 Hz and 400 Hz, and there is a stable response around 50 Hz, which is the first harmonic of flywheel at 3000 r/min. The maximum response occurs in group #5 combined condition, and the image shift in y direction reaches 0.0275 pixels. The amplitude here is mainly contributed by y flywheel (about 3300 r/min), and the other typical peaks are less than 0.01 pixels.

4.2. Discussion

The image motion information of the combined condition includes all the information of the typical response of single-flywheel spinning. When speed of z flywheel is 3000 r/min, the micro-vibration caused by the first harmonic of flywheel at 50 Hz appears in almost all results of the combined condition. Such as, when the speed of y flywheel is 3300 r/min, the typical image shift response caused near 334.5 Hz exists in the combined working conditions including the flywheel frequency and speed. Fig. 8 and Fig. 9 shown that the system image motion excited by micro-vibration is mainly concentrated are above 10 Hz.

Some micro-vibration response information of combined condition does not exist in the results of single flywheel working condition. For example, the image motion at 324 Hz and 453.6 Hz in combined condition #1 cannot be observed in the superposition single flywheel condition. It may be due to the coupling effect of the three flywheels when combined spinning, which stimulates the characteristic frequency that does not exist under a single flywheel spinning condition. Furthermore, it can be found that 324 Hz is near the axial translational modal frequency of the flywheel. It can be considered that the three-flywheels spinning combined, so that the axial translational modes are coupled and amplified, resulting in the characteristic response of the image shift at 324 Hz. The characteristic response at 453.6 Hz is caused by the combined action of 9.06-subharmonics (@3000 r/min) and 10.06-subharmonics (@2700 r/min) of the flywheel.

In the test results of single flywheel working conditions of three flywheels, small amplitude can be observed near 453.6 Hz. Among which the image shift of x flywheel in a speed of 2700 r/min is 0.00164 pixels, as for y flywheel and z flywheel with speeds of 3000 r/min, the image shift generated near this frequency are both of 0.00096 pixels. The combined action of three flywheels leads to the typical image motion phenomenon near the frequency of 453.6 Hz.

In most cases, the amplitude of typical response after linear superposition of single flywheel conditions is basically equal to the combined results, and in some cases, the image motion results are less than the test results of combined condition.

5. Conclusions

A new quasi-zero stiffness device with adaptive adjustment and variable stroke, which is actually a double pendulum system, was proposed. And image motion and experimental study of a 0.1″ space pointing measuring instrument for micro-vibration conditions were studied. The first-order frequency of the quasi-zero stiffness device is 0.114 Hz and the second-order frequency is 0.295 Hz. This device can effectively provide low stiffness to test the 0.1″ space pointing measuring instrument under micro-vibration of different spacecraft attitudes. The design improves the system efficiency. The system image motion excited by micro-vibration is mainly concentrated above 10 Hz. The image motion caused by one-single flywheel is no more than 0.015 pixels, which is mostly produced by the modal resonance of space pointing measuring instrument between 300 Hz and 400 Hz. Under the condition of multiple flywheels combined spinning, the micro-vibration response caused by each flywheel has certain coupling and amplification characteristic, meanwhile the maximum peak value is still not greater than 0.03 pixels in frequency domain. In addition, there may be some coupling effect in the combined rotation process of flywheel, which excites the characteristic frequency that does not exist in the single flywheel condition. These new findings will be helpful in theoretical and technical support for the development of spacecraft with 0.1″ pointing requirements.

Declaration of Competing Interest

The authors declare that they have no known competing financial interests or personal relationships that could have appeared to influence the work reported in this paper.

References

1. Yuan L, Wang MM, Wu YP, et al. Review on development of space starlight measurement technology. *Acta Aeronaut Astronaut Sinica* 2020;**41**(8):7–18, 2 [Chinese].
2. Li L, Yuan L, Wang L, et al. Recent advances in precision measurement & pointing control of spacecraft. *Chin J Aeronaut* 2021;**34**(10):191–209.
3. Li W, Huang H, Zhou X, et al. Design and experiments of an active isolator for satellite micro-vibration. *Chin J Aeronaut* 2014;**27**(6):1461–8.
4. Zhou W, Li D, Luo Q, et al. Analysis and testing of microvibrations produced by momentum wheel assemblies. *Chin J Aeronaut* 2012;**25**(4):640–9.
5. Li L, Tan L, Kong L, et al. The influence of flywheel micro vibration on space camera and vibration suppression. *Mech Syst Signal Process* 2018;**100**:360–70.
6. Wu Y, Zheng M, He W, et al. High precision attitude dynamic tracking control of a moving space target. *Chin J Aeronaut* 2019;**32**(10):2324–36.
7. Li L, Wang L, Yuan L, et al. Micro-vibration suppression methods and key technologies for high-precision space optical instruments. *Acta Astronaut* 2021;**180**:417–28.
8. Hadar O, Dror I, Kopeika NS. Real-time numerical calculation of optical transfer function for image motion and vibration. Part 1: Experimental verification. *SPIE Proceedings-8th Meeting on Optical Engineering in Israel: Optical Engineering and Remote Sensing* 1993;566–78.
9. Gong XX, Zhang L, Xuan M. Modeling and ground-based experimental jitter researches on earth observation satellite. *Acta Photon Sin* 2019;**48**(3): 312004.

10. Wu D, Xie T, Lu M, et al. Modeling and experimental study on the micro-vibration transmission of a control moment gyro. *IEEE Access* 2019;**7**:80633–43.

11. Yu Y, Gong X, Zhang L, et al. Full-closed-loop time-domain integrated modeling method of optical satellite flywheel micro-vibration. *Appl Sci* 2021;**11**(3):1328.

12. Gong XX, Zhang L, Xuan M. Numerical modeling method for evaluation of image motion caused by flywheel disturbances. *Acta Photon Sin* 2019;**48**(5): 528002.

13. Chen S, Xuan M, Xin J, et al. Design and experiment of dual micro-vibration isolation system for optical satellite flywheel. *Int J Mech Sci* 2020;**179**:105592.

14. Wu YJ, Sun X, Fan JJ, et al. Micro-vibration test and analysis of refrigeration for visible and infrared integrated space camera. *Conference on telescopes, space optics and instrumentation* 2020.

15. Li L. Flywheel micro-vibration mechanism and suppression integrated study for high resolution optical satellite [dissertation]. Changchun: University of Chinese Academy Sciences; 2018 [Chinese].

16. Zhang H, Li S, Liu S, et al. Coupled microvibration analysis of space optical load platform. *AIAA J* 2018;**56**(9):3766–75.

17. Liu MH, Cao H, Liu C, et al. Micro-vibration test of high resolution spacecraft. *J Phys: Conf Ser* 2021;**1877**(1): 012021.

18. He G, Wang X. Real-time micro-vibration measurement in sinusoidal phase-modulating interferometry. *Optik* 2009;**120**(3):101–5.

19. Tao Y, Wang M, Xia W. Semiconductor laser self-mixing micro-vibration measuring technology based on Hilbert transform. *Opt Commun* 2016;**368**:12–9.

20. Ma L, Wang YY, Hong Y, et al. Novel spacecraft on-orbit ultra-static weightlessness environment simulation test system. China patent CN 2016110745433. 2016 Nov 29.

21. Shen JF, Zhong M, Jiang GW, et al. Satellite micro-vibration test multi-point suspension system and design method. China patent CN 2013103500194. 2015 Jul 15.

22. Jia XZ, Zhang L, Zhong X, et al. Testing device for effect of satellite platform micro-vibration on camera imaging. China patent CN 2016100584789. 2016 Apr 27.

23. Lu ZQ, Shao D, Ding H, et al. Power flow in a two-stage nonlinear vibration isolation system with high-static-low-dynamic stiffness. *Shock Vib* 2018;**2018**:1697639.

24. Liu J, editor. *Lecture Notes on Theoretical Mechanics.* Singapore: Springer Singapore; 2019.

25. Elaichi T, Zebbiche T. Stagnation temperature effect on the conical shock with application for air. *Chin J Aeronaut* 2018;**31**(4):672–97.

26. Wang H, Wang Y, Li Z, et al. Systematic centroid error compensation for the simple Gaussian PSF in an electronic star map simulator. *Chin J Aeronaut* 2014;**27**(4):884–91.